Bulletin of the
Seismological Society of America

Vol. 71 August 1981 No. 4

EFFECTS OF FAULT FINITENESS ON NEAR-SOURCE GROUND MOTION

By Ralph J. Archuleta and Stephen H. Hartzell*

ABSTRACT

Near-source ground motion at four azimuths but constant epicentral range is computed from a buried circular strike-slip fault in a half-space. Particle acceleration, velocity, and displacement at each station on the free surface is computed in the frequency band 0.0 to 5.0 Hz. The assumed dislocation is derived from the Kostrov (1964) displacement function for a continuously propagating stress relaxation. The azimuthal variations in the amplitudes and waveforms directly result from spatially varying slip on the fault, spatially varying radiation pattern over the fault, and the magnitude and direction of the rupture velocity. The near-source ground motions are dominated by the rupture in the direction of the receiver.

Using a 100-bar effective stress (initial stress minus sliding friction) in a Poisson solid with β = 3.0 km/sec the shear wave speed, and shear modulus $\mu = 3.0 \times 10^{11}$ dyne/cm^2, the simulated earthquake has a moment $M_0 = 4.5 \times 10^{25}$ dyne-cm. Using a rupture velocity of 0.9β, the peak acceleration is 1195 cm/sec^2 and velocity 104 cm/sec for the receiver directly on strike. For a receiver 30° off strike, the maximum acceleration 236 cm/sec^2 occurs on the vertical component.

Introduction

Concepts such as receiver distance, radiation pattern, and arrival times of P and S waves are well defined when the receiver is far enough that the radiation appears to emanate from a single point. When the receiver is near the source, such that the radiation originates over some area or volume, the above far-field quantities are ill defined. No longer is there one distance between source and receiver or a single coefficient to describe the effect of a radiation pattern. Consequently the ground motion cannot be interpreted using the same approach that was appropriate for the far-field. In recent years, the data base of strong ground motion records from sites near moderately large earthquakes has greatly increased. Most notable is the strong motion record set for the 15 October 1979 Imperial Valley earthquake (Brady *et al.*, 1980). To analyze such records, a clear understanding is needed of the complications that arise when one is no longer in the far-field but situated close to a finite rupture. The fault model discussed here is a relatively simple one, but it includes the important effects of fault finiteness, directivity, the stopping phase, and the free surface.

This paper discusses how the spatial extent of the fault influences the near-source ground motion, in particular the high-frequency components of ground motion. At

* Present address U.S. Geological Survey, 345 Middlefield Road, Menlo Park, California 94025.

each step in the computations, parameters are chosen that maintain an upper frequency resolution of 5 Hz. The ground motion—particle acceleration, velocity, and displacement—is computed for a buried circular source in a three-dimensional semi-infinite medium, employing fault mechanics based on the slip function for a constant propagating stress drop (Kostrov, 1964). The wave propagation is based on the Green's functions for a semi-infinite linearly elastic isotropic homogeneous medium (Johnson, 1974). Parameters that strongly affect the azimuthal variation of near-source motion are spatially varying slip on the fault, spatially varying radiation pattern, and rupture velocity. Finally, to examine other approaches for calculating near-source ground motion, the model results are compared with the analytic solution for a propagating stress relaxation using a program developed by Richards (1973) and with a finite element method developed by Archuleta and Frazier (1978).

Description of Fault Model

The fault is a buried vertically oriented circular plane in a homogeneous isotropic linearly elastic half-space (Figure 1). The radius of the fault is 5 km; the center is at a depth of 7 km. The faulting is pure strike-slip with only slip parallel to the strike

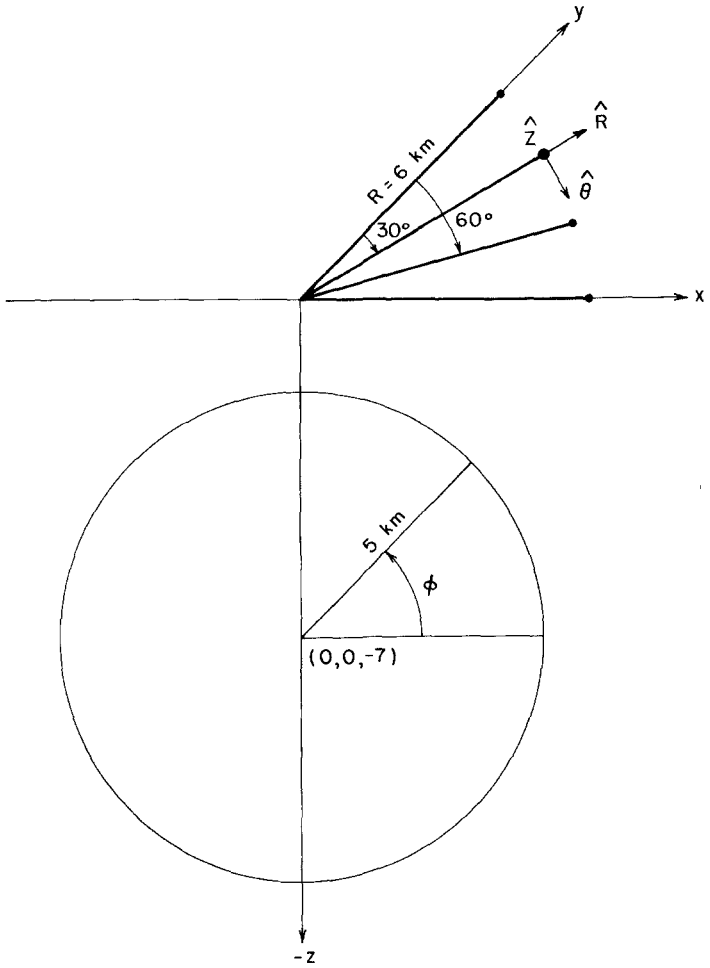

Fig. 1. Geometry of fault and receivers with orthogonal unit vectors $\hat{R}, \hat{\theta}, \hat{Z}$ indicating the components of particle motion.

allowed. The kinematics of the source are based on the Kostrov slip function for a constant stress drop and a constant rupture velocity (Kostrov, 1964). Since the Kostrov slip function is valid for a continuously expanding fault, the slip function is modified to account for the finiteness of the fault, as discussed below.

Slip is initiated at the center of the fault; the rupture spreads radially with a constant velocity 0.9β, where β is the shear wave speed of the medium. When the rupture reaches the outer circumference of the fault, a healing front is initiated that propagates from the circumference toward the center with velocity β, a velocity consistent with numerical simulations of dynamic faulting (Day, 1979). At the instant this healing front reaches a given point on the fault plane, the slip velocity is set to zero, thereby fixing the dislocation amplitude. Similar approaches have been taken by Bouchon (1978) and Boatwright (1980) although these investigators use a P-wave speed to heal the fault. An illustration of this slip velocity function at a radius of 2.5 km is shown in Figure 2. The Kostrov slip velocity, expressed as

$$\dot{s}(\underline{\xi}, t) = C(v/\beta)\frac{\sigma_E}{\mu}\frac{\beta t H(t - r/v)}{\sqrt{t^2 - r^2/v^2}} \tag{1}$$

is singular at the arrival time of the rupture front. In this expression, $C(v/\beta)$ is a number depending on the rupture velocity (Dahlen, 1974; Richards, 1976), σ_E the effective stress (the difference between the initial stress and sliding friction), μ the shear modulus, v the rupture velocity, H the Heaviside function, r the radius, and t the time. To remove this singularity, the slip function is analytically convolved with a boxcar of width 0.03 sec (also shown in Figure 2). Since convolution with a boxcar is equivalent to low-pass filtering, a 0.03-sec width preserves frequencies up to 10 Hz. The amplitude spectrum of the boxcar is shown in the *lower left* of Figure 2. The final slip velocity function and its corresponding displacement amplitude spectrum are shown in the *upper* and *lower right*, respectively, of Figure 2.

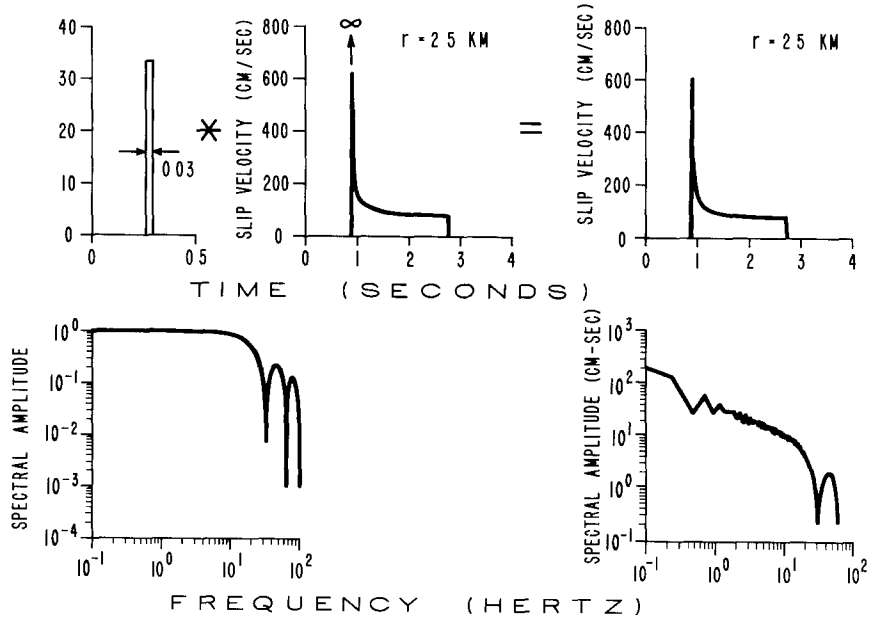

FIG 2. A schematic diagram illustrating the construction of the slip rate function for a concentric ring at a radius of 2 5 km. Spectral amplitude of the corresponding slip function shown at the *lower right*

The method of computation of synthetics proceeds by discretizing the fault plane with point sources and convolution with $\dot{s}(\underline{r}, t)$. We take advantage of the circular symmetry in $\dot{s}(\underline{r}, t)$ to limit the number of convolutions. Since every point on the fault plane at a constant radial distance from the point of nucleation has the same slip-velocity function, the fault plane is segmented into a series of concentric rings. Each ring is represented by a series of point sources evenly spaced at 100 m. The distance between the centers of each adjacent ring is also 100 m. The 5-km-radius fault consists of 50 rings with a total of 7,722 point sources. The half-space Green's functions $u_\iota(\underline{r}', t')$ (Johnson, 1974) are computed for each point source on a given ring and summed with the appropriate phase delays corresponding to the rupture-time and the travel-time delays to a preselected receiver on the free surface. Figure 3 diagrams the corresponding 50 modified Kostrov slip-velocity functions. The synthetic displacement, $u(\underline{x}, t)$, for the entire circular fault model is given by

$$u(\underline{x}, t) = \sum_{\iota=1}^{50} \dot{s}_\iota(\underline{r}, t') * \frac{d}{dt} u_\iota(\underline{r}', t') \tag{2}$$

where the summation index ι is over the number of rings, $*$ indicates convolution, and the displacements $u_\iota(\underline{r}, t)$ are computed for a constant ramp source-time function. Both $u_\iota(\underline{r}, t)$ and $u(\underline{x}, t)$ are sampled at an interval of 0.008 sec. The point-source spacing of 100 m is therefore the limiting factor in the coherent frequency

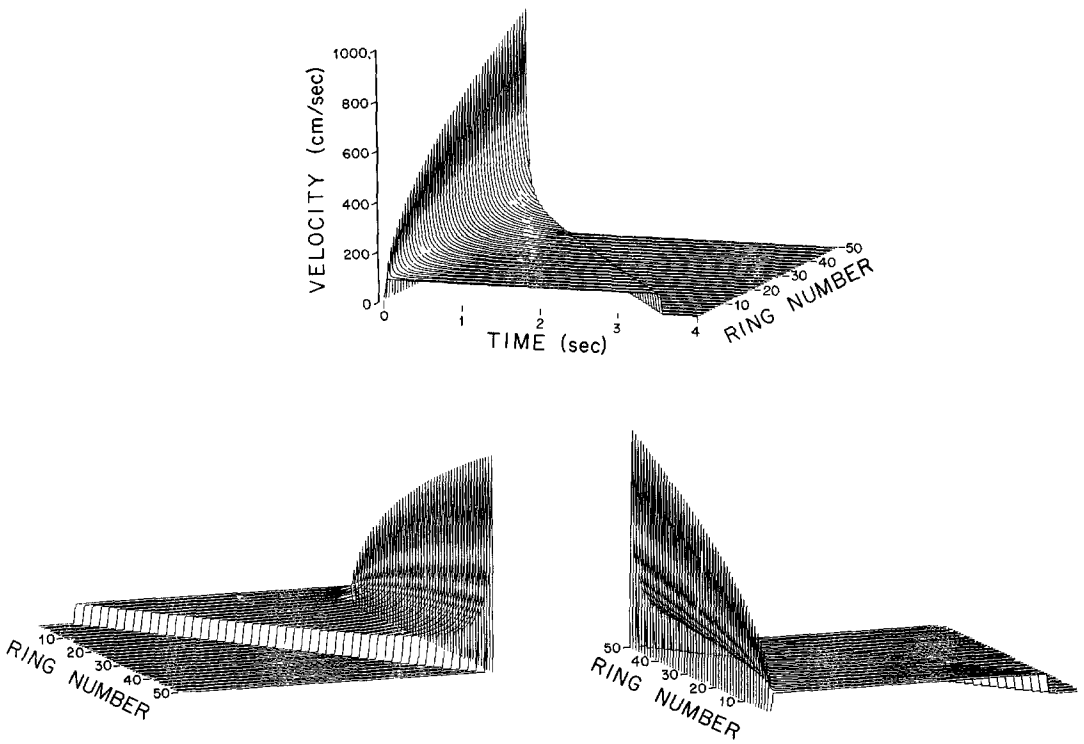

FIG 3 Modified Kostrov velocity functions on fault. Each ring has a different slip rate function. The slip rate over the fault is shown from three different angles: *upper figure*, from the vantage of looking out from the center, *lower left*, looking from the outer radius in, *lower right*, looking out from the center but emphasizing the initiation phase

content of the source. Using the coherent rupture condition of six source points per wavelength, the fault model considered here appears as a coherent rupture up to a frequency of 5 Hz ($f = \beta/\lambda$ = 3 km/sec/0.6 km = 5 Hz).

For each field point, the particle displacement is directly computed. The particle velocity and acceleration are then computed by numerically differentiating the particle displacement. In order to reduce any high-frequency noise caused by the numerical differentiation, a two-pole low-pass Butterworth filter, corner frequency at 5 Hz, is applied following each differentiation. The filter is applied in such a way that no phase shift is introduced. In spite of the 5-Hz filter, the synthetics presented in this paper still have some high-frequency ringing. This ringing is produced by the band-limited frequency content of the synthetics; it is generally of low amplitude. The maximum amplitudes of acceleration are sensitive to the filter's corner frequency; however, the maximum velocity and displacement are only slightly increased by moving the corner frequency to higher values (Hartzell, 1978).

The physical constants that have been used are: $\mu = 3.0 \times 10^{11}$ dyne/cm^2, $\beta = 3.0$ km/sec, $\alpha = \sqrt{3}\,\beta$ where α is the P-wave speed of the medium, $v = 2.7$ km/sec, and $\sigma_E = 100$ bars. It is important to note that all values of particle displacement, velocity, and acceleration scale directly with the effective stress, σ_E, (Madariaga, 1976). The effective stress, the difference between the initial stress and the stress due to sliding friction, is the stress available to accelerate the opposite sides of the fault plane. If the final stress is equal to the sliding frictional stress on the fault plane, then the effective stress is equal to the stress drop. Stress drop estimates Hanks (1977) has compiled for a large number of earthquakes, show that the stress drops lie in the range 1 to 100 bars. The choice of an effective stress of 100 bars, then, is a reasonable one. The average dislocation amplitude on a circular fault is given by

$$\bar{D} = \frac{2}{3} D_{\max} = \frac{2}{3} C(v, \beta)\left(\frac{r}{v} + \frac{r}{\beta}\right) = 190 \text{ cm} \tag{3}$$

where $C(v, \beta) = 0.81$ for $v = 0.9\beta$. The seismic moment, $M_0 (= \mu \bar{D} A)$, is then 4.5×10^{25} dyne-cm. Using a moment-magnitude relation ($\log M_0 = 1.5\, M_L + 16$) determined by Thatcher and Hanks (1973), we compute $M_L = 6.4$ for this simulated earthquake.

Synthetic Time Histories

Synthetic time histories of particle acceleration ($\ddot{u}$), velocity ($\dot{u}$), and displacement (u) are shown in Figures 4 to 6. Each field point is at an epicentral distance of 6 km but at four different azimuths; 0°, 30°, 60°, and 90°, measured from the normal to the fault (Figure 1). Since we are discussing a finite source, the terms "radial" and "azimuthal" strictly apply only for sources that lie on the vertical axis bisecting the fault. Nonetheless we have resolved the particle motion into the orthogonal components $\hat{R}$, $\hat{Z}$, and $\hat{\theta}$ as shown in Figure 1.

The time axes in Figures 4 to 6 start at the origin time of the earthquake. The hypocenter is 9.22 km from each station. The first P wave arrives at 1.77 sec; the first S wave arrives at 3.07 sec. The rupture front reaches the 5-km boundary in 1.85 sec; the healing front reaches the center 3.52 sec after origin time. The minimum and maximum distances between the fault boundary and each receiver are: 6.32 km, 13.42 km (0°); 5.81 km, 13.64 km (30°); 4.78 km, 14.04 km (60°); and 4.22 km, 14.22 km (90°). Let ϕ be the angle measured counter-clockwise from the horizontal in the

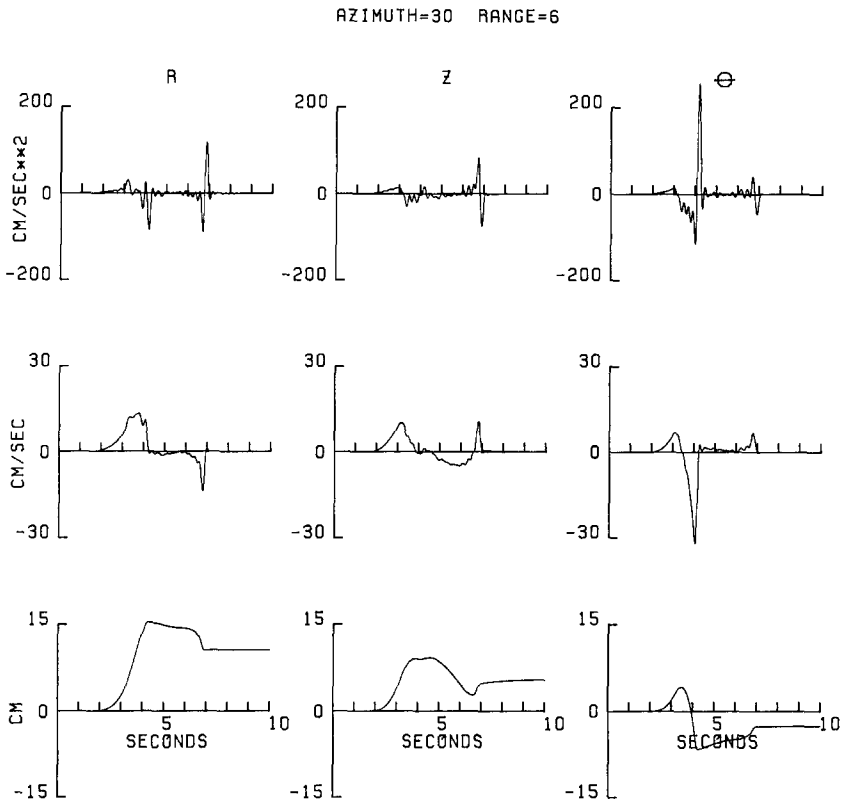

FIG 4 Synthetic three-component ground motion for a receiver at 30° and epicentral range of 6 km. $v = 0.9\beta$, 0.0 Hz $\leqq f \leqq$ 5.0 Hz

plane of the fault (see Figure 1). The value of ϕ that locates a radius vector along which points in the fault plane are closest to a given receiver are as follows: $\theta = 0°$, $\phi = 90°$; $\theta = 30°$, $\phi = 66.8°$; $\theta = 60°$, $\theta = 53.4°$; $\phi = 90°$, $\phi = 49.4°$. Knowing the rupture velocity, wave speeds, and certain distances, it is possible to identify certain arrivals. However, as we point out below, the particle motion cannot be analyzed fully in terms of discrete arrivals of particular waves.

Collectively, the synthetic three-component ground-motion plots (Figures 4 to 6) show the azimuthal dependence of the waveforms and amplitudes for each component of motion. The differences in the time histories at various azimuths result from several complicating factors related to the finite spatial extent of the fault. The factors that strongly influence the ground motion are (1) spatially varying radiation coefficients, (2) time and spatial dependence of the slip function, and (3) the interrelation among rupture velocity, elastic wave speeds and hypocentral distance between the receiver and different points on the fault plane.

Radiation coefficient

The clearest example of the effect of the spatially varying radiation coefficient is the θ component ("*SH*" radiation) at 30° and 60°, Figures 4 and 5, respectively. For a point source at the center of the fault, in fact, any point on the $-z$ axis, the *SH* radiation factor is equal but opposite in sign at 30° and 60° (Aki and Richards, 1980). At 60°, the receiver is closer to the projected strike of the fault to the free

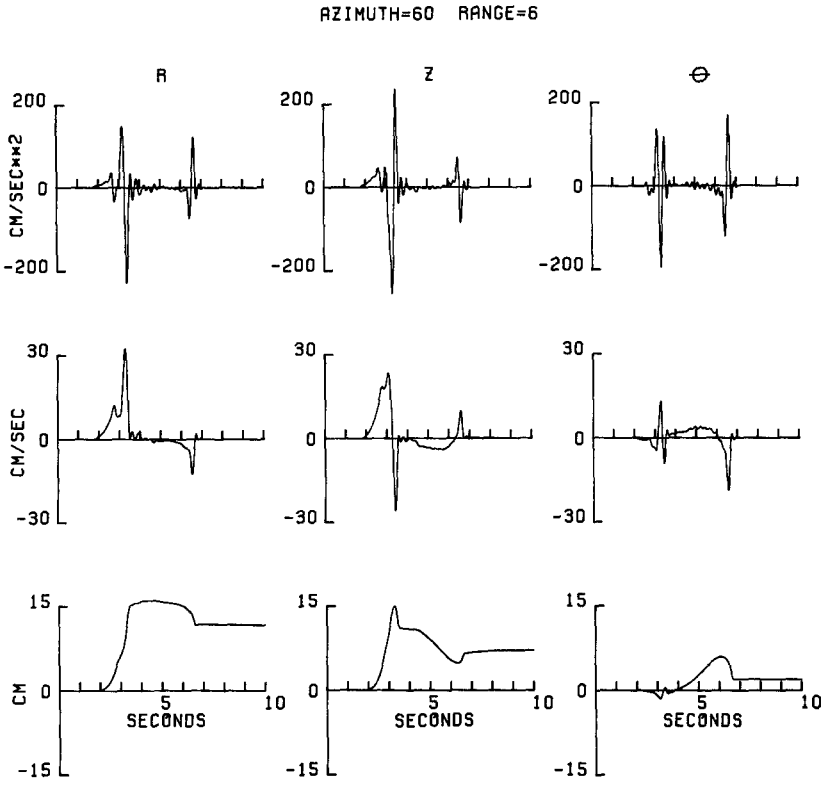

FIG 5 Synthetic three-component ground motion for a receiver at 60° and epicentral range of 6 km $v = 0.9\beta$, 0 0 Hz $\leqq f \leqq$ 5.0 Hz.

surface, and one might expect larger particle velocity and acceleration than for a receiver at 30°, compare, e.g., the θ component at 90° and 0° (Figure 6). Yet the opposite is true. Also at 60°, the amplitude of the first S waves (3.07 sec) is subdued, and there is one more zero crossing of the waveform than at 30°. The cause of this complexity lies with the SH radiation coefficient.

Any point source not along the $-z$ axis is not oriented with an angle of 60° or 30° with respect to the particular receiver. As the rupture spreads over the fault the radiation coefficient continuously changes. To show how this affects the amplitude and waveform, the SH coefficient is computed for different points on the fault plane and projected onto the θ direction. The values of the SH radiation coefficient that contribute to the θ component of motion at 60° are shown in Figure 7. The numerical values are equally spaced at 1 km on the fault plane. Note that the first arriving S waves will come primarily from the *upper right quadrant*, closest to the receiver. In this quadrant, the SH coefficient changes sign, causing the waves to interfere destructively. This interference not only diminishes the amplitude but also produces a waveform that has an extra oscillation. Waves arriving later from the *lower left quadrant* have larger coefficients but also travel a greater distance with a commensurate decrease in amplitude due to geometrical spreading. A similar figure can be constructed for a receiver at 30°. In that case, the entire *upper right quadrant* has negative coefficients. Hence the S waves first arriving at a receiver at 30° interfere constructively, thereby producing a one-sided pulse with larger amplitude than at 60°.

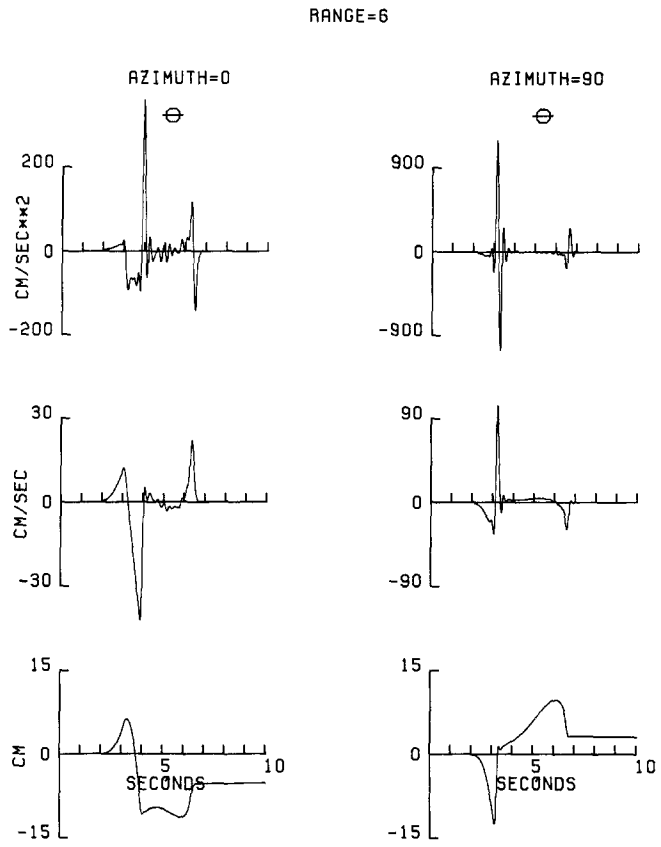

FIG 6. Synthetic ground motion for receivers at 0° and 90° and epicentral range of 6 km $v = 0.9\beta$, 0.0 Hz $\leqq f \leqq$ 5.0 Hz.

Slip-rate function

The spatial dependence of the slip rate function (Figure 3) is critical. As the rupture grows, those points on the fault farthest from the nucleation have the largest peak-in-slip rate, which occurs at the arrival time of the rupture front. From this maximum, the slip rate decays with the square root of time to a finite value equal to that at the nucleation point. At the arrival of the healing phase from the boundary of the fault, the slip rate goes to zero instantaneously. As a consequence, the slip velocities for those points near the boundary have large amplitudes and narrow pulse widths. For a particular receiver, the section of annulus near the boundary of the fault and closest to the receiver greatly influences the amplitude of the particle acceleration, as noted by Madariaga (1979) for far-field waveforms. For example, the maximum acceleration of the θ component (Figure 4) results from radiation arriving about 0.7 sec after the first S wave. Owing to the slip rate being set to zero at the boundary, this time corresponds with the expected arrival of the first arriving S wave, i.e., the first S wave radiated by healing of the fault. In Figure 5, the pronounced second peak at about 3.4 sec for the radial and vertical components also appears to originate from the boundary of the fault closest to the receiver. As discussed in the next section, the isolation of a particular phase from any specific point on the fault, except for the hypocenter, is not a practical form of analysis because of the mixing of arrivals from various parts of the fault.

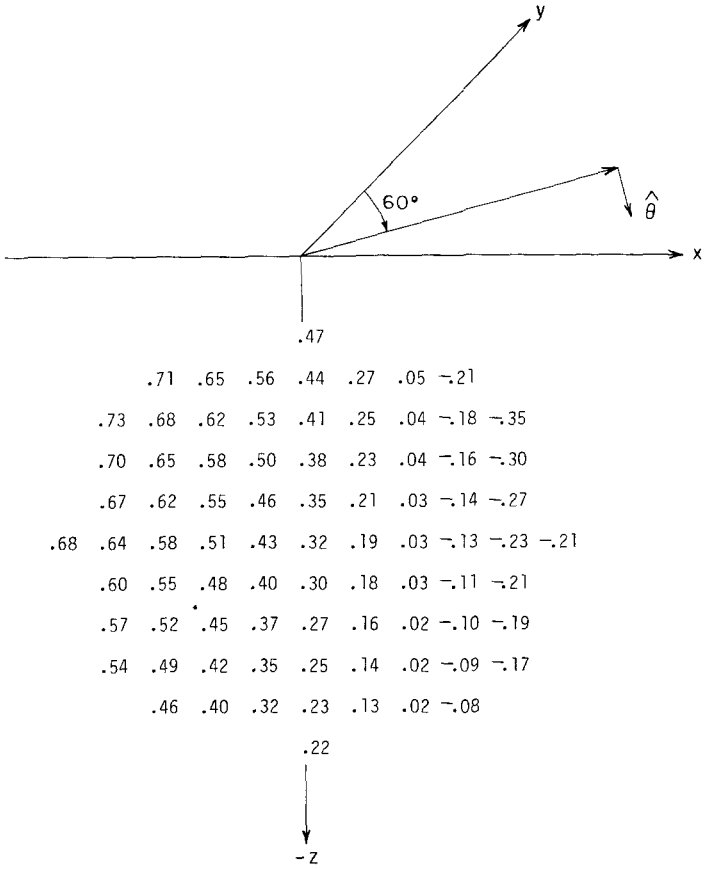

FIG. 7 Numerical values of the *SH* radiation coefficient on the fault that contribute to the θ component of motion for the receiver at 60° The numerical values are equally spaced at 1.0-km intervals.

Another important parameter is the slip rate's own time dependence. Unlike the simple ramp-slip function, which radiates only at its beginning and end, the slip function used here radiates continuously from beginning to end. Except for points near the boundary, the slip function used, unlike a ramp, is highly asymmetric in that the initiation of slip radiates more than the healing, compare, e.g., the amplitudes of initiation and healing in Figures 2 or 3.

Fault size, rupture velocity, and wave speeds

For a given point source and receiver, quantities such as arrival times of P and S waves, receiver distance, and radiation coefficients are well defined. For a receiver in the proximity of a finite fault, those quantities lose their unique interpretation. In order to gain more insight into what part of the fault is contributing to the synthetic seismogram, the arrival times of S waves from different points on the fault are computed. T_S, the arrival time for S wave radiation from the leading edge of the slip rate function, i.e., radiation from the initiation phase, is given by

$$T_S = R(r, \phi, \theta)/\beta + r/v \tag{4}$$

where R is the distance between a point on the fault at radius r and angle ϕ and a particular receiver. In terms of epicentral distance e (6 km), hypocenter depth d (7

km), and angles θ and ϕ shown in Figure 1,

$$R^2 = d^2 + e^2 + r^2 - 2\,dr \sin\phi - 2er \cos\phi \sin\theta. \tag{5}$$

For the initiation phase, r is simply equal to vt. S-wave radiation from the trailing edge of the slip rate function, i.e., the healing phase, arrives at time T_H given by

$$T_H = R(r*, \phi, \theta)/\beta + r*/\beta \tag{6}$$

where

$$r* = r_{\max} - \beta(t - r_{\max}/v) \tag{7}$$

with r_{max} equal to the final radius of the fault. The arrival times, T_S and T_H, for the four receivers are plotted as a function of the angle ϕ measured in the fault plane (Figure 8). To interpret Figure 8, one must be in a (t, ϕ) coordinate system, where the radius is time and the angle ϕ sweeps around the fault. Each concentric line is separated by 0.1 sec. Concentric circles in (r, ϕ) space on the fault are mapped into closed loops of (t, ϕ) at the receiver. With a hypocentral distance of 9.22 km and shear wave speed of 3.0 km/sec, the first S wave arrives at 3.07 sec. Consequently, for the first 3.07 sec, no arrival times are plotted in Figure 8, a to d. Since the hypocenter is the same distance to a receiver for all angles ϕ, the arrival time is a circle. The circles become distorted as time increases, reflecting the fact that even though the rupture front remains a circle on the fault, the points on that circle at different angles ϕ are at different distances from the receiver. Consequently, radiation arrives at different times. The inner collection of closed loops are arrival times from the initiation phase. The outer collection of loops, which appear to be the inner collection rotated by 180°, are the arrival times resulting from the healing of the rupture. Note that the final arrival time of the healing phase is also a circle since the last point on the fault to heal is the hypocenter.

As illustrated by Figure 8, the energy released in the quadrant closest to the receiver and the quadrant where the rupture is propagating toward the receiver arrives at the receiver within a very short time interval; whereas energy released for the initiation phase in the quadrant farthest from the receiver arrives later in time and spreads out over a large time interval. The width of the pulse originating from the section of the fault propagating toward the receiver is approximately $r_{\max}(1/v - 1/\beta \sin\Psi)$, where $r_{\max}$ is the final radius and Ψ the angle between the receiver and the fault plane. Because the rupture nucleates at depth, a receiver at $\theta = 0°$, 40° (Ψ) off the fault plane, also is affected by directivity. In short, the pulse width at a receiver is controlled by directivity related to a propagating rupture. The healing phase shows the same effect, but now the healing is moving away from the receiver for azimuths, ϕ, on the fault closest to the receiver. The more distant parts of the fault show the energy being concentrated into a narrow pulse because the healing phase originates at the boundary and moves inward to the center. The pulse is narrower, since the fault heals at the S-wave speed.

Once the rupture reaches the final radius and healing is initiated, there exists a time interval in which both initiating and healing phases are arriving from different parts of the fault, e.g., a radius vector of 5 sec in Figure 8 that sweeps all 360° will intersect both initiation and healing arrival times. The radiation from an initiation phase is of one sign whereas the healing phase has an opposite sign. When initiation and healing phases arrive simultaneously, they tend to cancel each other. Note that

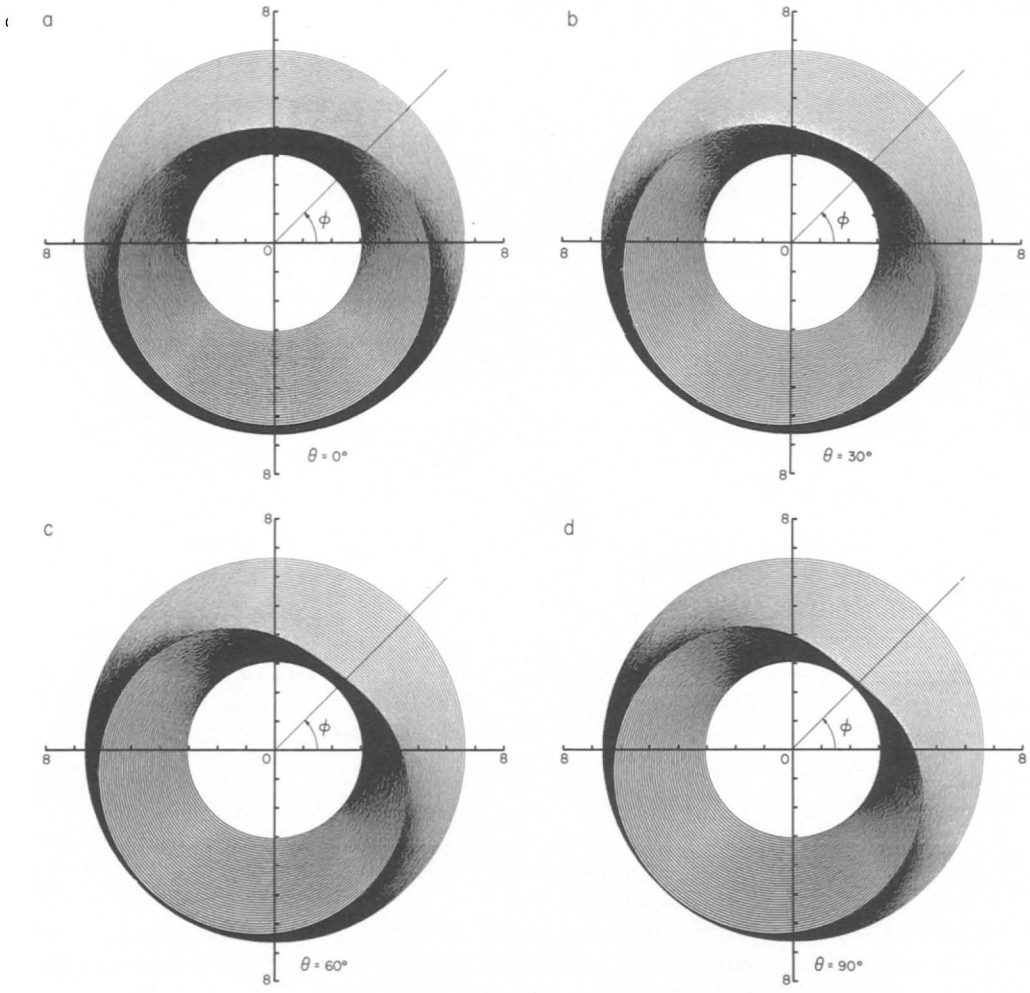

FIG. 8. The arrival time for *S*-wave radiation from the initiation and healing phases for successive concentric rings on the fault. *Inner loops* are from initiation, *outer loops* from healing. The direction of the rupture and healing relative to the station are evident. Receiver azimuths are indicated by θ, $v = 0.9\beta$.

the pulse width of the first arriving energy at the receiver (the *dark region* in the *upper right quadrant*) becomes narrower as the receiver changes from 0° to 90°, where the directivity effect is maximum.

The effect of directivity depends not only on the angle between the direction of rupture propagation and the receiver but also on the absolute value of the rupture velocity (Ben-Menahem, 1961). As an indication of the degree to which the rupture velocity affects the ground motion, synthetics were calculated for a rupture velocity of 0.75β. The synthetic time histories for receivers at 60°, 0°, and 90° shown in Figures 9 and 10 can be compared directly with time histories in Figures 5 and 6. The maximum values are listed in Table 1. The most striking contrast is the particle acceleration at 90° for $v = 0.9\beta$ (Figure 6) and for $v = 0.75\beta$ (Figure 10). The maximum positive amplitude of 1165 cm/sec^2 at 90° has been reduced 74 per cent to 311 cm/sec^2 when $v = 0.75$. The negative swing (−1060 cm/sec^2) in the particle acceleration at 90° for $v = 0.9\beta$ reduces to −443.5 cm/sec^2 for $v = 0.75\beta$. The particle

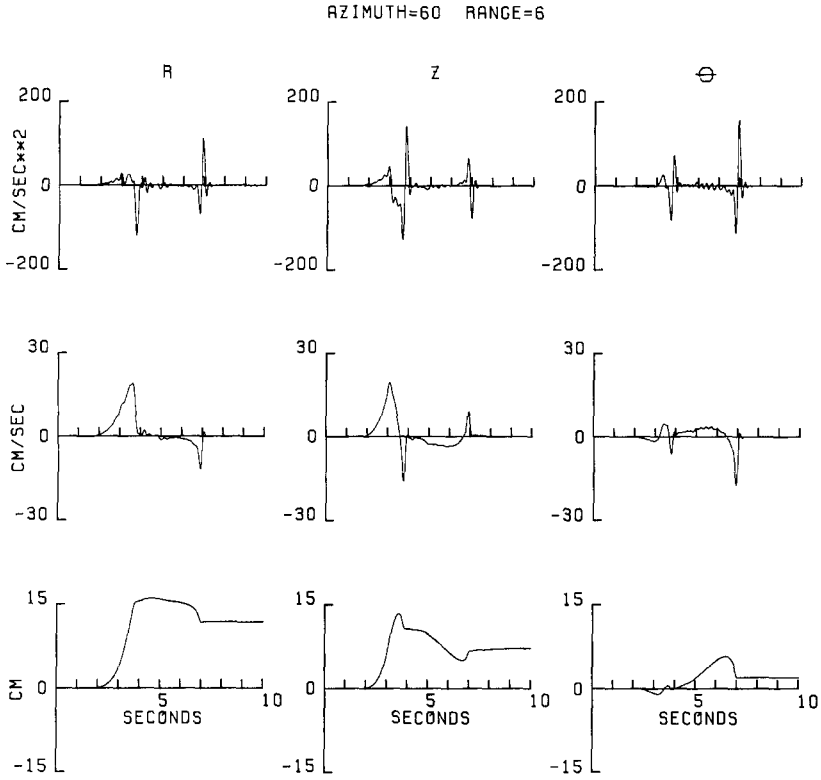

FIG. 9 Synthetic three-component ground motion for a receiver at 60° and epicentral range of 6 km $v = 0.75\beta$, 0.0 Hz $\leqq f \leqq$ 5.0 Hz.

velocity is reduced by 50 per cent, and the particle displacement by 32 per cent for the same phases in the time histories.

The changes in ground-motion amplitudes for ruptures with speeds of 0.9β and 0.75β are the most obvious. More subtle differences are seen in the waveforms themselves. The stopping phase arriving at about 7 sec appears larger relative to the initiation phase at about 3 sec because the healing criterion has not been changed. Although the displacement pulses are similar, the acceleration waveforms are much different. Compare, e.g., the radial components in Figures 5 and 9. In Figure 5, the leading positive pulse at ~3 sec is nearly the same as the following negative swing, whereas in Figure 9 only the negative swing appears prominent. This change in direction of the phase is attributed to the abrupt stopping of the slip function at the boundary closest to the receiver. A similar comparison can be made for the θ component. In general, the slower rupture velocity affects the character and amplitude of the first arriving phases. Almost no discernible differences exist for phases arriving later from other parts of the fault.

Seismic and engineering implications

Because of the source finiteness, many of the methods used for far-field analysis of seismograms are inapplicable for ground motion recorded in the near-source region. Consider the θ component in Figure 5. Near-field accelerometers would record the motion, but due to instrumental bandwidth, no zero frequency motion would be recorded. This makes it impossible to obtain the displacement record shown in Figure 5. The velocity would most likely be recovered in total. If one were

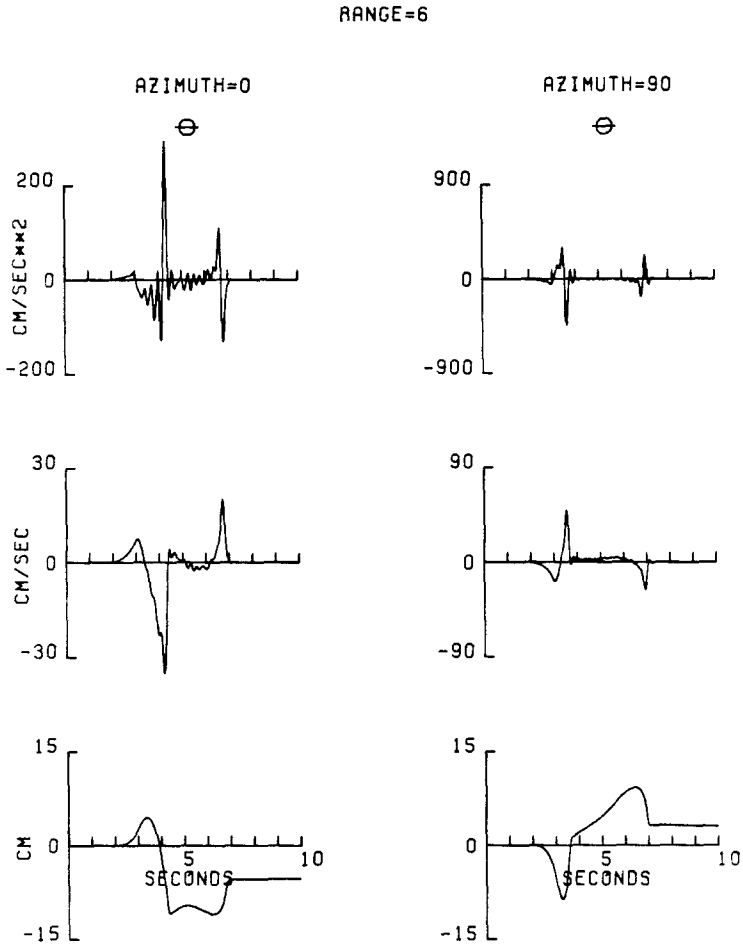

FIG 10 Synthetic ground motion for receivers at 0° and 90° and epicentral range of 6 km. $v = 0.75\beta$, $0.0 \text{ Hz} \leqq f \leqq 5.0 \text{ Hz}$.

to take the clean velocity pulse between 3 and 4 sec to construct a Brune (1970) displacement spectrum by Fourier transforming and postmultiplying by one over the angular frequency, the analysis would lead to gross errors in estimates of the source radius and stress drop. Basically, the radiation producing the velocity pulse does not come from a single point. More important, the pulse is a measure of only that radiation from the section of the fault that propagates toward the receiver. Even if one rigorously accounts for directivity, errors will arise from insufficient knowledge of the radiation coefficient and of the varying distance between source and receiver. These considerations exist for a simple fault in a half-space. If the earth's structure is included, the results obtained by far-field analysis of near-source records would be highly questionable.

In engineering applications, the response spectrum is generally tied to the peak acceleration. In Table 1, we list the maximum values of particle acceleration, velocity, and displacement for each component at the various azimuths, again numerical values are based on a 100-bar effective stress. An earthquake with a 50-bar effective stress and the same rupture velocity in an identical medium would produce values half as large. Although the synthetics of particle acceleration accurately include frequencies only up to 5 Hz, the peak acceleration is 1195.6 cm/

TABLE 1

MAXIMUM VALUES OF PARTICLE ACCELERATION (u), VELOCITY (u), AND DISPLACEMENT (u) IN CM/SEC^2, CM/SEC, AND CM AT VARIOUS AZIMUTHS

			$v = 0.9\beta$			
		60°			30°	
	u	u	u	u	u	u
R	−228 6	32 4	16 1	128.7	18.4	15.3
Z	236.2	26 9	14 9	88.7	12 0	9.6
θ	−194.4	−18.8	6.0	329 2	−41.7	5.8
		0°			90°	
	u	u	u	u	u	u
θ	359.8	−42 2	−11.4	1195.6	104.4	−12.6
			$v = 0\ 75\beta$			
		60°			30°	
	u	u	u	u	$\dot{u}$	u
R	−118 5	19 0	16.1	118.3	−13.8	15.3
Z	141.2	19.5	13.3	83 1	10.6	9.2
θ	157.3	−17.3	5 7	256.9	−31 9	−6 7
		0°			90°	
	u	u	u	$\dot{u}$	u	u
θ	297 0	−35.1	−10.9	−443.5	50.2	9 3

sec^2 for the horizontal component at 90°. This large value results from the receiver being directly along the strike of the rupture, where the effect of directivity is maximized. Off the fault the peak values are of the order of 300 cm/sec^2. The values in Table 1 include no attenuation. If a simple Q correction [exp $(\omega t/2Q)$] with Q = 150 is applied, the peak accelerations are reduced about 10 per cent; the velocity and displacement are practically unchanged. The peak acceleration is extremely sensitive to the filter parameters (Hartzell, 1978). The peak particle velocity and displacement are much more stable measures relative to frequency content. Finally, it is worth pointing out that at 60° the vertical acceleration is the largest of the three components. Earthquakes such as Gazli, USSR, Coyote Lake, California, and Imperial Valley, California, all have the maximum recorded acceleration on the vertical. Although these recorded accelerations may have been caused by the local structure, the synthetics at 60° show that even without structure, the vertical component of acceleration at a particular site can be the maximum acceleration even where the earthquake is pure strike slip.

Self-similar and finite-element comparisons

The basis for the slip rate function used in this paper is the self-similar model described by Kostrov (1964). The constant stress drop model is for a circular rupture

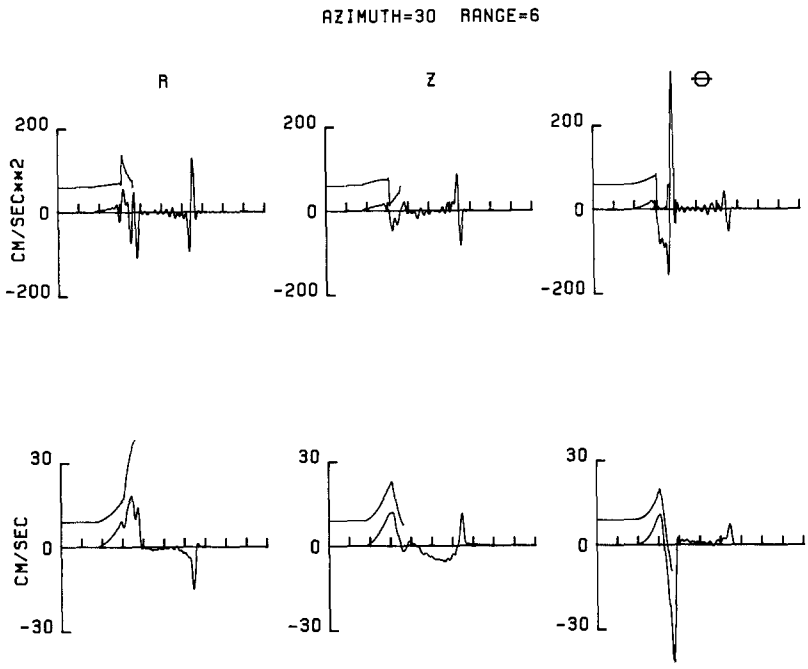

FIG 11 Particle velocity and particle acceleration comparison between the analytic solution of a propagating stress relaxation and synthetic ground motion computed in this paper. Analytic solution is shown offset above the synthetic. $\theta = 30°$, epicentral range 6 km, $v = 0.9\beta$, 0.0 Hz $\leqq f \leqq$ 5.0 Hz

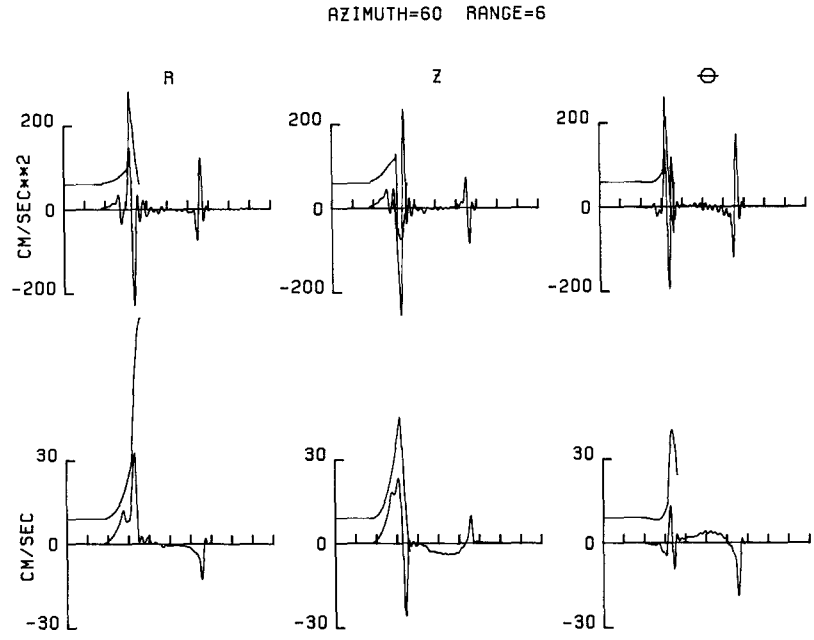

FIG. 12. Same as Figure 11 for $\theta = 60°$

that expands continuously in a full-space. If the effects of the free surface are ignored, the fault model is a self-similar rupture for the first second following the arrival of the P wave from the hypocenter. For a receiver at 60°, the closest edge of the fault boundary is 4.78 km. A P wave arrives at the receiver from the edge at 2.77 sec (t = 5.0 km/2.7 km/sec + 4.78 km/5.2 km/sec). The first P wave from the hypocenter arrives at 1.77 sec (9.22 km/5.2 km/sec). For 1 sec after the P wave arrival, the particle motion from the self-similar rupture and the numerical synthet-

ics presented here, should agree except for effects due to the free surface. Figures 11 and 12 compare the analytic and numerical results for the particle acceleration and velocity for θ at 30° and 60°, respectively. The analytic solution, shown offset above the numerical results, was computed using a program written by Richards (1973) wherein analytic solution has been filtered in exactly the same manner as our synthetics. To approximate the free surface, the amplitudes of the self-similar calculation have been doubled. The agreement, especially for acceleration, is close. The S- to P-wave conversion at the free surface and the first arrival of the stopping phase from the outer annulus produce the most marked differences. Nevertheless, the analytic solution is a valuable indicator of the amplitude and waveform of the first motion to be expected from the initial part of the rupture process. Although the analytic solution is filtered so that a valid comparison could be made, the analytic solution is not limited in its frequency content and could be used as diagnostic of amplitudes for coherent ruptures when discussing higher frequency ground motions that are expensive to compute using other numerical techniques.

Another approach to computing near-source ground motions from a propagating stress relaxation over an areal fault in a half-space is a finite element method (Archuleta and Frazier, 1978), a dynamical model of the source in that the slip function directly results from a stress relaxation. The slip function is not prescribed as in the fault model described earlier. The finite element method also has the capability for incorporating different frictional constitutive relations and various rheological properties. This method, though, is limited in practice to the low-frequency part of the ground motion. Figures 13 and 14 compare the finite element results, the offset trace, and the kinematic results. Because of frequency limitations in the finite element method, all the results are low passed with a corner frequency of 0.5 Hz. In the frequency range considered, the particle velocity and displacement are in excellent agreement.

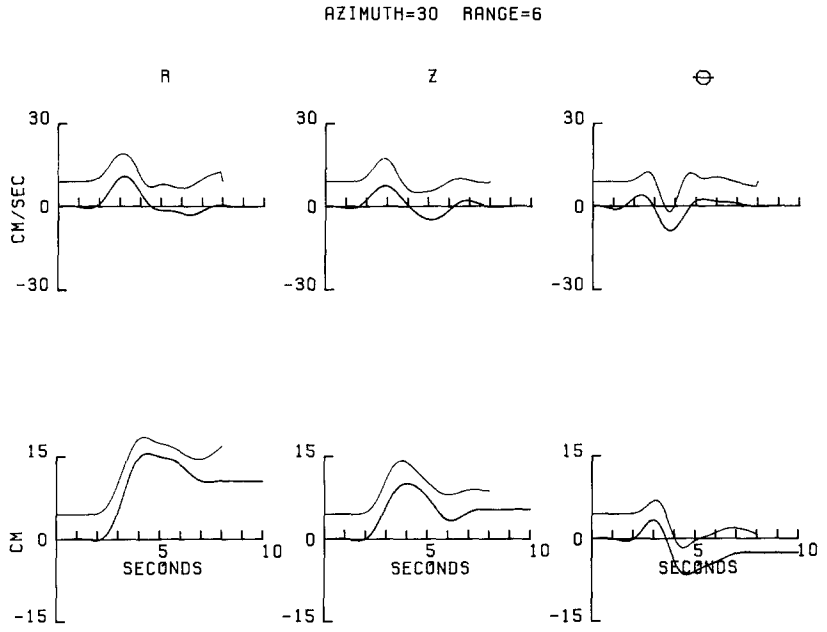

FIG 13 Particle velocity and particle displacement comparison between a finite element computation and the corresponding synthetic ground motion computed in this paper. Finite-element computation is shown offset above the synthetic $\theta = 30°$, epicentral range 6 km, $v = 0.9\beta$, 0 0 Hz $\leqq f \leqq$ 0.5 Hz.

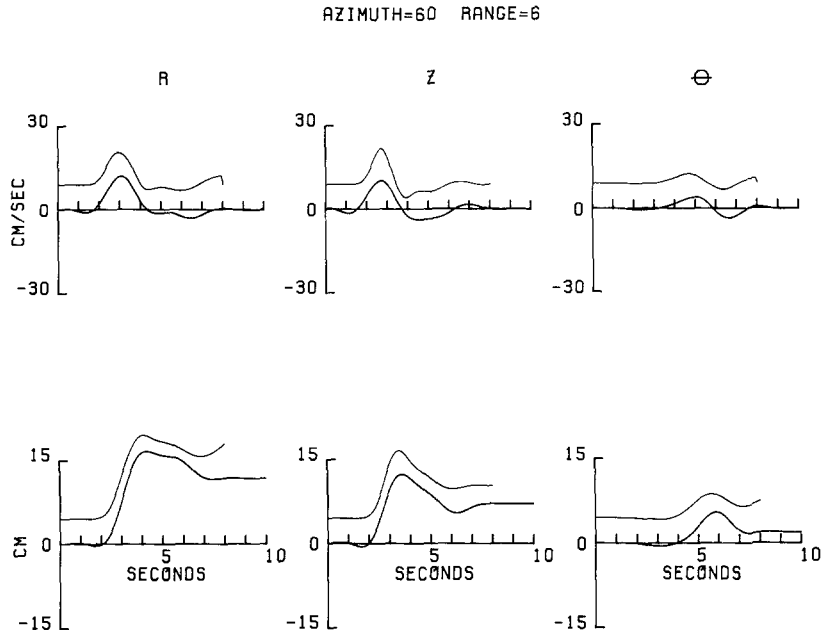

FIG 14. Same as Figure 13 for $\theta = 60°$.

Although the particle displacement has not changed much in waveform or amplitude, the particle velocity has clearly undergone a significant change. In this low-frequency range, the details of faulting have been smeared to such a degree that the effects of the spatial extent of the fault are almost lost. The greatest change is for the θ component at 60° (Figure 14). The whole character of the 5-Hz pulse (Figure 5) is lost, and the only hint of the fault's spatial effect is the lower amplitude of the $\hat{\theta}$ component relative to $\hat{R}$ and $\hat{Z}$.

DISCUSSION

Based on the idea that an earthquake is a propagating stress relaxation over some finite area, a kinematic source model has been constructed. The slip, equivalently the slip rate, is based on the analytic solution of a propagating stress relaxation (Kostrov, 1964). To account for the finiteness of the fault, a healing phase is introduced. From this kinematic description of faulting, near-source ground motion is computed in the frequency band 0.0 to 5.0 Hz.

In analyzing the different aspects of the azimuthal variation of the near-source ground motion, it was found that the spatial extent of the faulting is preeminent in determining the waveforms and amplitudes. The main factors are the spatially varying slip rate function, spatially varying radiation pattern coefficient, the rupture velocity magnitude and direction relative to the receiver, and the constructive and destructive interference of radiation arriving from different parts of the fault. Although these factors complicate the total time history of near-source ground motion, the first arriving radiation, principally a measure of the duration of rupture in the direction of the receiver, dominates the ground motion. Real earthquakes occur in a much more complicated stress and geologic environment, both of which can severely alter the near-source recordings. Nevertheless, the near-source "*SH*" particle velocity time histories from the California earthquakes—1966 Parkfield (station 2), 1971 San Fernando (Pacoima dam), 1979 Coyote Lake (Gilroy Array station 6), and the 1979 Imperial Valley (El Centro Array stations 6 and 7)—are

remarkably similar in their waveforms (Figure 15). In degrees measured clockwise from the north, the direction of positive horizontal particle velocity for each station is: Parkfield, 245°; Pacoima, 346°; Gilroy 6, 230°; El Centro 6, 230°; and El Centro 7, 230°. The polarity of the phases depends, of course, on the relative position between the epicenter and the station. In the 1966 Parkfield earthquake, e.g., the epicenter was north of station 2, and the rupture propagated southward toward station 2. In the 1979 Imperial Valley earthquake the epicenter was south of stations 6 and 7, and the rupture propagated north. Both were right-lateral strike-slip events. The time history for each event is dominated by a clean pulse whose width is substantially narrower than the time it would take for a rupture having velocity less than the shear wave speed to traverse the length of the assumed faulted area.

Although the simulated earthquake can be analyzed in terms of corner frequency

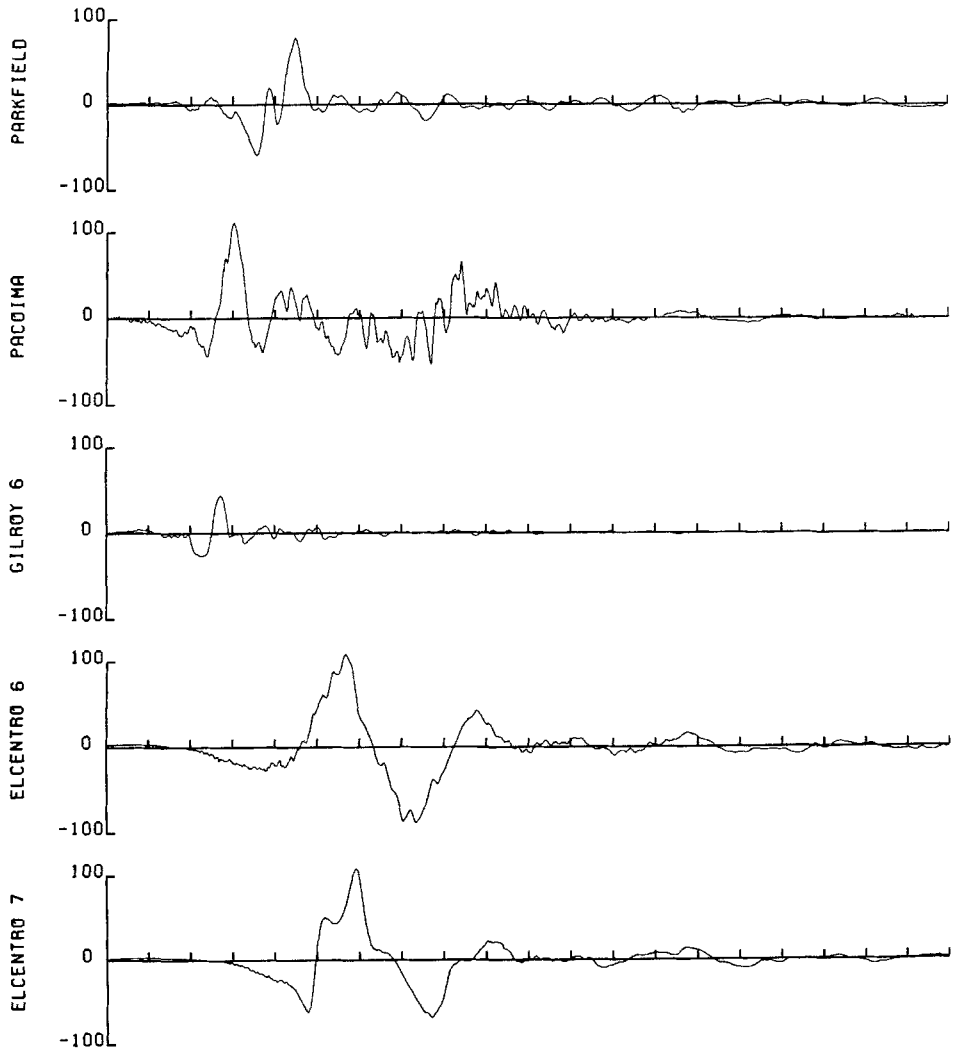

FIG 15. Five near-source horizontal particle velocity time histories from California earthquakes (in descending order) 1966 Parkfield; 1971 San Fernando, 1977 Coyote Lake, and 1979 Imperial Valley For each earthquake the accelerograph was located directly in line with the strike or dip of the fault. With respect to the notation in this paper, the component of motion plotted is θ for $\theta \cong 90°$. The amplitude scale is in cm/sec Each tic mark is 1 sec

and displacement spectrum for receivers far from the source in a half-space (Hartzell, 1978), the same type of analysis applied to near-source records is fraught with erroneous assumptions. For the ground motion computed in this paper, each detail of the source, propagation path, and receiver location is precisely known. Nevertheless the interpretation of the waveforms is not a straightforward or easy process. In cases of real earthquakes where very little is known about the source or the medium, the explanations of the near-source ground motion can be multitudinous. This is not to imply that near-source ground motion is uninterpretable but rather that interpretations of near-source ground motion should take into account effects due to the finiteness of the fault.

Acknowledgments

The authors wish to thank John Boatwright and Tom Hanks for preliminary review of this paper We are grateful for the assistance of Norman Abrahamson and John Ketchens in executing the plot programs for most of the figures Part of this work was done on behalf of the Office of Nuclear Regulatory Research, U.S Nuclear Regulatory Commission

References

Aki, K and P. G. Richards (1980). *Quantitative Seismology Theory and Methods*, volumes I and II, W H Freeman and Company, San Francisco, p 115

Archuleta, R. J and G. A Frazier (1978) Three-dimensional numerical simulations of dynamic faulting in a half-space, *Bull Seism Soc Am* **68,** 541–572.

Ben-Menahem, A (1961) Radiation of seismic surface waves from finite moving sources, *Bull. Seism Soc Am* **51,** 401–435.

Boatwright, J. (1980). A spectral theory for circular seismic sources; simple estimates of source dimension, dynamic stress drop, and radiated energy, *Bull Seism Soc Am* **70,** 1–27

Bouchon, M (1978). A dynamic source model for the San Fernando earthquake, *Bull. Seism Soc Am.* **68,** 1555–1576

Brady, A G , V. Perez, and P N Mork (1980). The Imperial Valley Earthquake, October 15, 1979 Digitization and processing of accelerograph records, *U S Geol. Surv., Open-File Rept. 80-703,* 1–309

Brune, J. N. (1970) Tectonic stress and the spectra of seismic shear waves from earthquakes, *J Geophys. Res* **75,** 4997–5009.

Dahlen, F. A. (1974) On the ratio of *P*-wave to *S*-wave corner frequencies for shallow earthquake sources, *Bull Seism. Soc. Am* **64,** 1159–1180.

Day, S. M (1979) Three-dimensional finite difference simulation of fault dynamics, Systems, Science and Software Report SSS-R-80-4295, 1–72.

Hanks, T C (1977) Earthquake stress drops, ambient tectonic stresses and stresses that drive plate motions, *Pageoph* **115,** 441–458

Hartzell, S. H. (1978) Interpretation of earthquake strong ground motion and implications for earthquake mechanism, *Ph.D Dissertation,* University of California at San Diego, 268 pp

Johnson, L. R (1974) Green's function from Lamb's problem, *Geophys J.* **37,** 99–131.

Kostrov, B V (1964). Self-similar problems of propagation of shear cracks, *J Appl. Math Mech.* **28,** 1077–1078

Madariaga, R. (1976). Dynamics of an expanding circular fault, *Bull. Seism. Soc Am.* **66,** 639–666.

Madariaga, R. (1979). Seismic radiation from earthquake models based on fracture mechanics, *Fracture Mechanics, SIAM-AMS Proceeding* **12,** 59–77.

Richards, P. G (1973). The dynamic field of a growing plane elliptical shear crack, *Intern J Solids Struct* **9,** 843–861.

Richards, P. G. (1976) Dynamic motions near an earthquake fault a three dimensional solution, *Bull Seism Soc Am* **66,** 1–32.

Thatcher, W and T. Hanks (1973). Source parameters of southern California earthquakes, *J. Geophys Res* **78,** 8547–8576.

U S. Geological Survey
345 Middlefield Road
Menlo Park, California 94025 (R.J.A.)

Seismological Laboratory
California Institute of Technology
Pasadena, California 91125 (S H H.)

Manuscript received November 14, 1980